



Universiteit  
Leiden  
The Netherlands

## Isotopes and the characterization of extrasolar planets

Zhang, Y.

### Citation

Zhang, Y. (2023, June 6). *Isotopes and the characterization of extrasolar planets*. Retrieved from <https://hdl.handle.net/1887/3619726>

Version: Publisher's Version

License: [Licence agreement concerning inclusion of doctoral thesis in the Institutional Repository of the University of Leiden](#)

Downloaded from: <https://hdl.handle.net/1887/3619726>


**Note:** To cite this publication please use the final published version (if applicable).

## 3

## The $^{12}\text{CO}/^{13}\text{CO}$ isotopologue ratio of a young, isolated brown dwarf

*Linking atmospheric characteristics of planets to their formation pathways is a central theme in the study of extrasolar planets. Although the  $^{12}\text{C}/^{13}\text{C}$  isotope ratio shows little variation in the Solar System, the atmosphere of a super-Jupiter was recently shown to be rich in  $^{13}\text{CO}$ , possibly as a result of dominant ice accretion beyond the CO snow line during its formation. Carbon isotope ratios are therefore suggested to be a potential tracer of formation pathways of planets. In this work, we aim to measure the  $^{12}\text{CO}/^{13}\text{CO}$  isotopologue ratio of a young, isolated brown dwarf. While the general atmospheric characteristics of young, low-mass brown dwarfs are expected to be very similar to those of super-Jupiters, their formation pathways may be different, leading to distinct isotopologue ratios. We analysed archival K-band spectra of the L dwarf 2MASS J03552337+1133437 taken with NIRSPEC at the Keck telescope. A free retrieval analysis was applied to the data using the radiative transfer code petitRADTRANS coupled with the nested sampling tool PyMultiNest to determine the isotopologue ratio  $^{12}\text{CO}/^{13}\text{CO}$  in its atmosphere. The isotopologue  $^{13}\text{CO}$  is detected in the atmosphere through the cross-correlation method at a signal-to-noise of  $\sim 8.4$ . The detection significance is determined to be  $\sim 9.5\sigma$  using a Bayesian model comparison between two retrieval models (including or excluding  $^{13}\text{CO}$ ). We retrieve an isotopologue  $^{12}\text{CO}/^{13}\text{CO}$  ratio of  $97_{-18}^{+25}$  (90% uncertainty), marginally higher than the local interstellar standard. Its C/O ratio of  $\sim 0.56$  is consistent with the solar value. Although only one super-Jupiter and one brown dwarf now have a measured  $^{12}\text{CO}/^{13}\text{CO}$  ratio, it is intriguing that they are different, possibly hinting to distinct formation pathways. Regardless of spectroscopic similarities, isolated brown dwarfs may experience a top-down formation via gravitational collapse, which resembles star formation, while giant exoplanets favourably form through core accretion, which potentially alters isotopologue ratios in their atmospheres depending on the material they accrete from protoplanetary disks. This further emphasises atmospheric carbon isotopologue ratio as a tracer of the formation history of exoplanets.*

---

 **Zhang, Y., Snellen, I. A. G., & Mollière, P. (2021) The  $^{12}\text{CO}/^{13}\text{CO}$  isotopologue ratio of a young, isolated brown dwarf. A&A, 656, A76.**

### 3.1 Introduction

Planet formation and evolution are expected to leave imprints on the observed spectra of exoplanets. In bridging the gap between the spectral characterisation and formation mechanisms, isotopologue ratios have been suggested as informative tracers of planet formation conditions and evolutionary history (Clayton & Nittler, 2004, Zhang et al., 2021a). In the Solar System, deuterium/hydrogen (D/H) ratios demonstrate significant variations across planets, comets, and meteorites (Altwegg et al., 2015). While the D/H ratios in Jupiter and Saturn are consistent with the protosolar value, Uranus and Neptune are found to be enhanced in deuterium (Feuchtgruber et al., 2013), which is attributed to a likely increased contribution from accretion of D-rich ices beyond the water snow line. The terrestrial planets Earth, Mars, and Venus have higher D/H ratios (Drake, 2005), indicating not only solid accretion, but also atmospheric loss. Therefore, isotope ratios in planetary atmospheres can reflect the material reservoir of the birth environment, the formation mechanism (via core accretion or gravitational collapse), the relative importance of gas or ice accretion, and the atmospheric evolution.

In contrast with D/H ratios, carbon isotope ratios are found to be roughly constant in the Solar System (Woods, 2009), and therefore they are less effective diagnostic tools. However, the recent measurement of the  $^{12}\text{CO}/^{13}\text{CO}$  isotopologue abundance ratio in an exoplanet may require a reassessment of its diagnostic value. The  $^{13}\text{CO}$  isotopologue was detected at a significance of  $6\sigma$  in the atmosphere of the super-Jupiter TYC 8998 b. Intriguingly, the atmosphere is reported to be  $^{13}\text{CO}$ -rich with a  $^{12}\text{CO}/^{13}\text{CO}$  abundance ratio of 31, which is significantly lower than the local interstellar standard at  $\sim 68$  (Zhang et al., 2021a). A formation outside the CO snow line with a large contribution from ice-accretion (as an analogy to the D-enrichment in Solar System planets) has been invoked to explain the enrichment. Since the Solar System planets are thought to be formed within the CO snow line, no substantial enrichment in  $^{13}\text{C}$  is expected, because the bulk of their carbon reservoirs originate from CO gas in the inner disk, where  $^{13}\text{C}$  is not enhanced. It therefore suggests that the atmospheric carbon isotopologue ratios could also shed light on the formation history of exoplanets, especially for the directly imaged populations, which are observed at wide orbits beyond the CO snow line.

Several carbon fractionation processes in molecular clouds, young stellar objects (YSOs), and protoplanetary disks are suggested to alter the CO isotopologue ratios in the birth environment of planets, including isotopic ion exchange reactions (Langer et al., 1984, Milam et al., 2005), isotope-selective photodissociation (Bally & Langer, 1982, Miotello et al., 2014, van Dishoeck & Black, 1988, Visser et al., 2009), and gas-to-ice isotopologue partitioning (Acharyya et al., 2007, Smith et al., 2015). Depending on the location of the proto-planets and the material (gas or ice) they accrete from the environment, the isotopologue ratios in the atmospheres may deviate from the ISM standard. Therefore, detailed modelling of carbon fractionation in protoplanetary disks coupled with planet formation models have the potential to locate the birthplace and identify the formation mechanism of planets, like suggested for carbon-to-oxygen (C/O) ratios (Cridland et al., 2020, Madhusudhan et al., 2014, Mordasini et al., 2016, Öberg et al., 2011). Moreover, combining evidence from different observables, such as  $^{12}\text{C}/^{13}\text{C}$ , D/H, and C/O ratios, allows for a more comprehensive understanding of the formation process.

Compared to the D/H ratios ( $\sim 10^{-5}$ ) which can potentially be probed via HDO/H<sub>2</sub>O

and  $\text{CH}_3\text{D}/\text{CH}_4$  (Mollière & Snellen, 2019, Morley et al., 2019), the  $^{12}\text{C}/^{13}\text{C}$  ratios ( $\leq 100$ ) are more readily detectable and attained from the ground with high-resolution spectroscopy targeting  $^{12}\text{CO}/^{13}\text{CO}$  (Mollière & Snellen, 2019). In addition to the recent result for a super-Jupiter, carbon isotopologue ratios have been measured toward various sources beyond the Solar System, including the interstellar medium (ISM) (Langer & Penzias, 1993, Milam et al., 2005, Yan et al., 2019), YSOs and protostars in gas and ices (Boogert et al., 2002, 2000, Jørgensen et al., 2018, 2016, Pontoppidan et al., 2005, Smith et al., 2015), giant stars, solar-type stars, and M dwarfs (Botelho et al., 2020, Crossfield et al., 2019b, Sneden et al., 1986, Tsuji, 2016), but not yet towards brown dwarfs. In this paper, we carry out a similar analysis to Zhang et al. (2021a) on archival high-resolution Keck/NIRSPEC data of a young, isolated brown dwarf. While its general atmospheric characteristics are expected to be very similar to those of super-Jupiters, its formation pathways may be different, leading to distinct isotopologue ratios. In addition, its spectrum can be studied at high signal-to-noise, and hence is more accessible.

We present the observations and spectrum extraction in Section 3.2, followed by a description of the retrieval model in Section 3.3. The retrieval results and the measurement of CO isotopologue ratio can be found in Section 3.4 and are discussed in Section 3.5.

Table 3.1: Properties of 2M0355, including those derived in this work.

Parameter	Symbol	Value
R.A. (J2000) <sup>a</sup>	$\alpha$	03:55:23.377
Dec. (J2000) <sup>a</sup>	$\delta$	+11:33:43.7
Distance (pc) <sup>a</sup>	$d$	$9.1 \pm 0.1$
Systemic velocity ( $\text{km s}^{-1}$ ) <sup>b</sup>	$v_{\text{sys}}$	$11.8 \pm 0.5$
Rotational velocity ( $\text{km s}^{-1}$ ) <sup>b</sup>	$v \sin(i)^*$	$14.7 \pm 2.3$
Spectral type <sup>c</sup>		L5 $\gamma$ /L3
2MASS K-magnitude (mag) <sup>d</sup>	$K_{\text{mag}}$	$11.526 \pm 0.021$
Age (Myr) <sup>e</sup>		$\sim 125$
Effective temperature (K) <sup>e</sup>	$T_{\text{eff}}$	$1430 \pm 40$
Mass ( $M_{\text{Jup}}$ ) <sup>f</sup>	$M_p$	$19^{+7}_{-5}$
Surface gravity (cgs) <sup>f</sup>	$\log g$	$4.69 \pm 0.15$
Carbon-to-Oxygen ratio <sup>f</sup>	C/O	$0.56 \pm 0.02$
CO isotopologue ratio <sup>f</sup>	$^{12}\text{CO}/^{13}\text{CO}$	$97^{+25}_{-18}$

\* our work indicates a smaller rotation velocity than found in the literature.

<sup>a</sup> Gaia Collaboration et al. (2018);

<sup>b</sup> Blake et al. (2010), Bryan et al. (2018);

<sup>c</sup> Cruz et al. (2009);

<sup>d</sup> Cutri et al. (2003);

<sup>e</sup> Aller et al. (2016), Faherty et al. (2013), Liu et al. (2013);

<sup>f</sup> this work.

## 3.2 Observations and spectrum extraction

2MASS J03552337+1133437 (hereafter 2M0355) is a free-floating, young brown dwarf discovered from 2MASS (Reid et al., 2008) and is likely a member of AB Doradus moving group (Liu et al., 2013). With a distance of 9.1 parsec and a spectral type of L5 $\gamma$  (with  $\gamma$  denoting a very low surface gravity), it is among the nearest and reddest L dwarfs (Cruz et al., 2009, Faherty et al., 2013). The properties of 2M0355 are summarised in Table 3.1. Its spectrum demonstrates signatures of low surface gravity and resembles those of directly imaged planetary mass objects, while being orders of magnitudes brighter and not contaminated by starlight. It is therefore an excellent target for high-resolution spectroscopic studies, providing insights into atmospheric properties under similar conditions to those of exoplanets.

### 3.2.1 Keck/NIRSPEC archival data

We used the archival K-band (2.03-2.38  $\mu\text{m}$ ) spectra of 2M0355 taken with the near-infrared spectrograph NIRSPEC ( $\lambda/\Delta\lambda \sim 25\,000$ ) at the Keck II 10 m telescope (McLean et al., 1998) on January 13, 2017. The data were obtained in natural seeing mode with a 0.432x24'' slit. The observations were performed with a standard ABBA nod pattern, resulting in 14 science exposures between 400 and 600 seconds, which amount to a total exposure time of two hours. The data have previously been used to measure the spin of the brown dwarf by Bryan et al. (2018).

As for the pre-processing, we first corrected the data using dark and flat field calibration frames, and then differenced each nodded AB pair to subtract the sky background. This led to 2D differenced images with two spectral traces (positive and negative) for each order. In the subsequent analysis, we focussed on the last two orders with the wavelength coverage of 2.27 - 2.31  $\mu\text{m}$  (blue order) and 2.34 - 2.38  $\mu\text{m}$  (red order), respectively. Subsequently, we straightened the 2D images on an order-by-order basis to align the curved spectral traces along the dispersion (x-)axis by fitting the traces with a third-order polynomial. Similarly, we also adjusted the spectral traces to correct for the tilted spectral lines on the y-axis due to instrument geometry. The tilt was measured by fitting the brightest sky line in the flat-fielded raw image with a linear function, which was then applied to the differenced frames. We then combined all the rectified 2D images to a single frame for each order.

From the combined 2D frames, we extracted 1D spectra for both the positive and negative traces, using the optimal extraction algorithm by Horne (1986). This method takes the weighted sum of the flux along the spatial dimension (the cross-dispersion axis), based on the empirical point spread function (PSF) constructed from the 2D frame, while rejecting outliers caused by cosmic rays or bad pixels. After obtaining 1D spectra for both traces, we add them up to form the master spectrum, resulting in an average signal-to-noise ratio (S/N) of  $\sim 35$  per unit of dispersion (pixel). This S/N value was estimated by comparing the master spectrum to a model spectrum obtained by the retrieval analysis (detailed in Section 3.3). Using the statistical flux uncertainties as calculated in the spectrum extraction process (accounting for shot noise and readout noise), we expect the S/N to be  $\sim 115$ , which differs from the former estimation by a factor of 3.3. This indicates the presence of correlated noise in the data and/or the imperfect modelling of telluric transmission and planetary spectra. Nevertheless, the S/N estimated via the comparison to models repre-

sents a lower limit to the data quality. We therefore base our further analysis on the assumption of this lower S/N.

To determine the wavelength solution for each order, we took advantage of the standard star spectra obtained under the same instrument configuration immediately before the observation, assuming that the wavelength solution remains the same. We compared the standard star spectrum with a telluric transmission model generated with ESO sky model calculator `SkyCalc`<sup>1</sup> (Jones et al., 2013, Noll et al., 2012) and fitted the wavelengths as functions of pixel positions using  $\sim 25$  telluric lines spread across each order with a third-order polynomial. This solution was then applied to the target spectrum.

We then used the ESO sky software tool `MoleculeFit` v3.0.1 (Smette et al., 2015) to perform telluric corrections on the master spectrum. The tool uses a line-by-line radiative transfer model (LBLRTM) to derive telluric atmospheric transmission spectra that can be fitted to observations. For model fitting, we selected two wavelength regions, 2.276 - 2.293  $\mu\text{m}$  and 2.347 - 2.382  $\mu\text{m}$ , which include strong telluric lines caused by  $\text{CH}_4$  and  $\text{H}_2\text{O}$ . The software accounted for the molecular abundances, instrument resolution, continuum level, and wavelength solution that can best fit observations. Using the best-fit Gaussian kernel width, we estimated the spectral resolution to be  $\lambda/\Delta\lambda \sim 27500$ . The atmospheric transmission model for the entire wavelength range was then derived based on the best-fit parameters. The model was removed from the master spectrum to obtain the telluric-corrected spectrum. Subsequently, we shifted the spectrum to the target's rest frame by accounting for the systemic and barycentric radial velocity. The flux was finally scaled to the K-band photometry of  $1.05 \times 10^{-14} \text{ W/m}^2/\mu\text{m}$  (Cutri et al., 2003). The scaling factor was determined by generating the planetary model spectrum at a larger wavelength coverage and then integrating the flux over the band pass of the K-band filter, and comparing it to the photometric value.

We note that measuring the CO isotopologue ratio requires careful calibration of the broad-band spectral shape. Because the CO absorption features span across the two spectral orders in the observations, the CO abundance inferred from the spectrum is sensitive to slight changes in the relative flux between the two orders. To calibrate this, we inspected spectra of two standard stars taken immediately before and after the target observations. We reduced the standard star spectra following the same procedure as described above and compared the telluric-corrected spectrum of the standard stars to a PHOENIX stellar model (Husser et al., 2013) with an effective temperature of 8200 K, as estimated for the stars (Gaia Collaboration et al., 2018). Since the standard star spectra are firmly in the Rayleigh-Jeans regime, potential uncertainties in effective temperature have negligible effects on the spectral shape. The comparison suggested that the observed flux ratio between the red and blue order was on average 3% higher than that of the model. We therefore decreased the flux in the red order by 3% to compensate for this.

The final spectrum of 2M0355 is shown in Fig. 3.1. The  $^{12}\text{CO}$   $v=2-0$  bandhead is clearly visible at 2.2935  $\mu\text{m}$ , while the first bandhead of  $^{13}\text{CO}$  at 2.3448  $\mu\text{m}$  falls outside of the detector. On the order of thirty  $^{13}\text{CO}$  lines are covered by the red order (see Fig. 3.2, left panel).

<sup>1</sup><https://www.eso.org/observing/etc/skycalc>

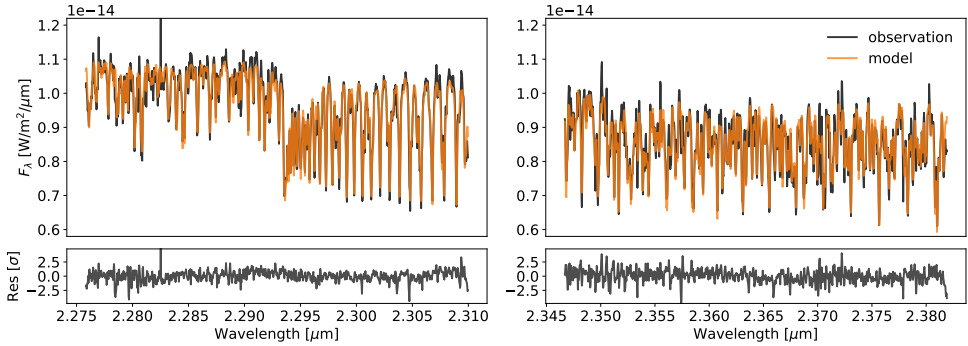


Figure 3.1: Last two orders (containing CO opacity) of the K-band spectrum of the brown dwarf 2M0355 taken with Keck/NIRSPEC. The orange line is the best-fit model with  $\log(g)=4.69$ ,  $[\text{Fe}/\text{H}]=0.2$ ,  $\text{C}/\text{O}=0.55$ , and  $^{12}\text{CO}/^{13}\text{CO}=97$ , obtained from the maximum likelihood model in the retrieval analysis. The bottom panel shows the residuals of the observed spectrum with respect to the model.

### 3.2.2 VLT/CRIRES+

We obtained high-resolution ( $\mathcal{R} = \lambda/\Delta\lambda \sim 80\,000$ ) emission spectra of 2M0355 at the K-band as part of science verification observations with the upgraded CRIRES at the VLT on September 19, 2021 under ESO programme 107.22TG. The observations were performed in seeing-limited mode with a standard ABBA nodding pattern, resulting in 4 science exposures of 300 seconds each. The data were taken at an airmass of 1.25 and a seeing of  $0.5''$ . The sky transparency is sub-optimal with variable, thick clouds.

The raw data were first reduced using the CRIRES pipeline to correct for bias, flat fielding, sky background, and bad pixels. We then used the intermediate data products to optimally extract the spectrum, taking into account the curvature of the spectral trace on the detectors. The wavelength solution was calibrated against a telluric transmission model generated with ESO sky model calculator `SkyCalc`<sup>2</sup> (Noll et al., 2012). We corrected for telluric absorption lines using `Molecfit` (Smette et al., 2015), and shifted the spectrum to the target’s rest frame.

## 3.3 Retrieval analysis

### 3.3.1 Atmospheric retrieval model

For our atmospheric free retrieval, in which all fitted parameters varied freely under the condition of chemical equilibrium but the temperature structure is unconstrained, we used a Bayesian framework composed of the radiative transfer tool `petitRADTRANS` (pRT) (Mollière et al., 2019) and the nested sampling tool `PyMultiNest` (Buchner et al., 2014), which is a Python wrapper of the `MultiNest` method (Feroz et al., 2009). Synthetic emission spectra are generated by pRT using a set of inputs, including the temperature structure, chemical abundances, and surface gravity. The `PyMultiNest` samples the parameter space and derives the posterior distribution of the fit.

The forward modelling consists of three major components: the temperature model, the chemistry model, and the cloud model. We parameterised the temperature-pressure

<sup>2</sup><https://www.eso.org/observing/etc/skycalc>

(T-P) profile using four temperature knots spaced evenly on a log scale pressure within 0.02 to 5 bar, where the contribution function of the observed spectrum peaks (see upper right panel in Fig. 3.3). The entire T-P profile was obtained by spline interpolation of the four temperature knots in the log space of pressure. The temperature profile outside this range is barely probed by the observations, and is simply considered to be isothermal in our model. There is no physical reasoning behind this T-P profile, and therefore few prior constraints are imposed on the solution.

The chemistry model used in our retrievals assumes chemical equilibrium as detailed in Mollière et al. (2020, 2017). In short, the chemical abundances are determined via interpolation in a chemical equilibrium table using pressure  $P$ , temperature  $T$ , carbon-to-oxygen ratio  $C/O$ , and metallicity  $[Fe/H]$  as inputs.

As for the cloud model, the same setup as in Mollière et al. (2020) is implemented using the Ackerman & Marley (2001) model. It introduces four additional free parameters: the mass fraction of the cloud species at the cloud base  $X_0^c$ , the settling parameter  $f_{sed}$  (controlling the thickness of the cloud above the cloud base), the vertical eddy diffusion coefficient  $K_{zz}$  (effectively determining the particle size), and the width of the log-normal particle size distribution  $\sigma_g$ . The location of the cloud base  $P_{base}$  is determined by intersecting the condensation curve of the cloud species with the T-P profile of the atmosphere.  $MgSiO_3$  and Fe clouds are expected to be the dominant cloud species in L dwarfs (Morley et al., 2012). Here, we only consider the  $MgSiO_3$  clouds, because Fe is not expected to be the dominant aerosol composition according to the microphysics model by Gao et al. (2020), and (even if the cloud forms) it condensates at a higher temperature which occurs at lower altitudes than the photosphere of the target.

### 3.3.2 Retrieving 2M0355

The cloudy retrieval model has 14 free parameters:  $R_p$ ,  $\log(g)$ ,  $[Fe/H]$ ,  $C/O$ ,  $^{12}CO/^{13}CO$ ,  $X_0^{MgSiO_3}$ ,  $f_{sed}$ ,  $K_{zz}$ ,  $\sigma_g$ ,  $v\sin(i)$  and four temperature knots for the T-P profile. The priors of these free parameters are listed in Table 3.2. We included  $H_2O$ ,  $CH_4$ ,  $NH_3$ ,  $^{12}CO$ , and the isotopologue  $^{13}CO$  as line opacity species. The model also accounts for the Rayleigh scattering of  $H_2$ , He, the collision induced absorption of  $H_2-H_2$ ,  $H_2-He$ , the scattering and absorption cross sections of crystalline, irregularly shaped  $MgSiO_3$  cloud particles.

We used the line-by-line mode of pRT to calculate the emission spectra at high spectral resolution. To speed up the calculation, we took every fifth point of opacity tables with  $\lambda/\Delta\lambda \sim 10^6$ . This sampling factor of 5 has been benchmarked against the original sampling to ensure unbiased inference of parameters. The synthetic high-resolution spectra were rotationally broadened by  $v\sin(i)$  and convolved with a Gaussian kernel to match the resolving power of the instrument ( $\lambda/\Delta\lambda \sim 27500$  for NIRSPEC and  $\lambda/\Delta\lambda \sim 80000$  for CRIREs+), then binned to the wavelength grid of the observed spectrum (2020 data points in total), and scaled to the observed flux according to  $R_p$  and distance of the target. The retrievals were performed by PyMultiNest in importance nested sampling mode with a constant efficiency of 5%. It uses 2000 live points to sample the parameter space and derives the posterior abundances.

In addition to the retrievals with individual dataset, we also performed joint retrieval using spectra taken with both spectrographs VLT/CRIREs+ and Keck/NIRSPEC. As the



Table 3.2: Priors and posteriors (90% uncertainties) of the 2M0355 retrievals.

Parameter	Prior	Posterior	Posterior2
$\log(^{12}\text{CO}/^{13}\text{CO})$	$\mathcal{U}(-12, 0)$	$-1.99 \pm 0.10$	$-2.03 \pm 0.09$
$R_p [R_{\text{Jup}}]$	$\mathcal{U}(0.3, 2.5)$	$0.97 \pm 0.02$	$1.13 \pm 0.03$
$\log(g)$ [cgs]	$\mathcal{U}(3.0, 6.0)$	$4.69 \pm 0.15$	$4.32 \pm 0.15$
[Fe/H]	$\mathcal{U}(-1.5, 1.5)$	$0.21 \pm 0.10$	$0.05 \pm 0.11$
C/O	$\mathcal{U}(0.1, 1.5)$	$0.56 \pm 0.02$	$0.55 \pm 0.02$
$T_0$ [K]	$\mathcal{U}(1500, 4000)$	$2322 \pm 138$	$2906 \pm 224$
$T_1$ [K]	$\mathcal{U}(0.5, 1)^*T_0$	$1731 \pm 17$	$1671 \pm 35$
$T_2$ [K]	$\mathcal{U}(0.5, 1)^*T_1$	$1640 \pm 18$	$1478 \pm 20$
$T_3$ [K]	$\mathcal{U}(0.5, 1)^*T_2$	$1452 \pm 21$	$1446 \pm 16$
$\log(\tilde{X}_0^{\text{MgSiO}_3})$	$\mathcal{U}(-2.3, 1)$	$-1.3 \pm 1.2$	-
$f_{\text{sed}}$	$\mathcal{U}(0, 10)$	$5.8 \pm 4.1$	$8.0 \pm 2.2$
$\log(K_{zz})$	$\mathcal{U}(5, 13)$	$10.5 \pm 3.2$	$10.0 \pm 1.8$
$\sigma_g$	$\mathcal{U}(1.05, 3)$	$2.0 \pm 0.8$	$1.89 \pm 0.82$
$\text{vsin}(i)$	$\mathcal{U}(0, 20)$	$2.0 \pm 1.3$	$1.2 \pm 1.3$
$\log(\tau_{\text{cloud}})$	$\mathcal{U}(0, 1)$	-	$0.02 \pm 0.03$

Posterior column shows values for the nominal model, while Posterior2 refers to the alternative model with enforced clouds.  $\mathcal{U}(a, b)$  represents a uniform distribution ranging from  $a$  to  $b$ . The  $\tilde{X}_0^{\text{MgSiO}_3}$  denotes  $X_0^{\text{MgSiO}_3}/X_{\text{eq}}^{\text{MgSiO}_3}$ , where  $X_{\text{eq}}^{\text{MgSiO}_3}$  is the mass fraction predicted for the cloud species when assuming equilibrium condensation at the cloud base location.

accurate calibration of the broad-band spectral feature is challenging in high-resolution observations, we discarded the absolute flux information by removing the low-frequency variation in both observations and models using a Gaussian smoothing filter with a width of 2 nm, only preserving the line-by-line variations. We included in our fit the near-infrared (2MASS and WISE) photometric measurements (Faherty et al., 2016) to assist constraints on the radius, temperature and surface gravity. The photometry was converted from magnitudes to fluxes using the species package<sup>3</sup> (Stolker et al., 2020). We observed in this analysis that the high-resolution spectra were more constraining than the photometric points, to the point where our retrieval would not correctly fit the SED if equal weighting is assigned to the photometry and the high-resolution data. On the other hand, we found that scaling the log-likelihood of the photometric data points by a factor of 100 ( $\sim \sqrt{\mathcal{R}_{\text{high}}/\mathcal{R}_{\text{photom}}}$ ) produced a good fit of both datasets. Although the validity of the procedure remains to be further studied, we note that the different weighting does not significantly affect the resulted isotopic ratios.

<sup>3</sup><https://species.readthedocs.io/>

## 3.4 Results

### 3.4.1 Retrieval results

The retrieval results are shown in Fig.3.3, including the retrieved temperature-pressure profile and the posterior distribution of the free parameters. The central values of the inferred parameters and their 90% uncertainties are summarised in Table 3.2, including  $^{12}\text{CO}/^{13}\text{CO} = 97_{-18}^{+25}$ ,  $\text{C/O} = 0.56_{-0.02}^{+0.02}$ ,  $[\text{Fe}/\text{H}] = 0.21_{-0.10}^{+0.11}$ ,  $\log(g) = 4.69_{-0.15}^{+0.15}$ , and  $R_p = 0.97_{-0.02}^{+0.03}$ . It suggests that 2M0355 has a solar C/O ratio and a super-solar metallicity. The inferred mass of  $19_{-5}^{+7} M_{\text{Jup}}$  is in line with previous estimations using evolutionary models based on its photometry and membership (age) of AB Dor moving group (Faherty et al., 2013). Using the evolutionary models for low-mass objects by Baraffe et al. (2015), we estimate the radius of a  $\sim 20M_{\text{Jup}}$  dwarf to be  $\sim 1.15R_{\text{Jup}}$  for an age of 120 Myr. The radius constrained from our retrieval model ( $\sim 0.97R_{\text{Jup}}$ ) is smaller than that expected from evolutionary tracks. This is likely associated with the temperature structure in the retrieval models. We note that the alternative retrieval model (described below) converges to different T-P profiles, leading to radii in agreement with the estimation from evolutionary models (see Table 3.2).

Moreover, we retrieved a much smaller rotational velocity ( $< 4 \text{ km s}^{-1}$ ) than the value ( $14.7 \text{ km s}^{-1}$ ) found by Bryan et al. (2018) using the same data, as listed in Table 3.1. Broadening synthetic spectra with a  $v\sin(i)$  of  $14.7 \text{ km s}^{-1}$  result in spectral lines too broad to fit the observation with a  $\lambda/\Delta\lambda \sim 27500$ . In our case, the widths of spectral lines are therefore dominated by the instrument resolution instead of the spin of the target. Regardless, the rotational broadening shows no impact on the inference of the isotopologue ratio.

Fig.3.3 shows that the properties of clouds are barely constrained. The inferred values of the parameters are similar to the cloud-free case that we tested, indicating that the retrieval converges to solutions with optically thin clouds. We suggest that this behaviour is a cooperative consequence of the freely adjustable temperature structure and properties of clouds. Since the presence of thick clouds can block the emission from high-temperature regions of the atmosphere below, the cloudy atmosphere is spectrally equivalent to the case of a cloudless atmosphere combined with a shallow (isothermal) temperature gradient. This effect has been put forward as an alternative (cloud-free) explanation for the red spectra of brown dwarfs and self-luminous exoplanets (Tremblin et al., 2016, 2015, 2017, 2019). Both cases provide good fits to the observed spectrum, but here the free retrieval model tends to converge to cloudless solutions, potentially because they occupy a larger volume in the parameter space than the cloudy solutions. The problem of too isothermal temperature structures in free retrievals of cloudy objects has also been discussed in Burningham et al. (2017), Mollière et al. (2020), and Burningham et al. (2021). Classical 1-d self-consistent calculations will predict a steeper temperature profile, requiring clouds to fit the data. It is therefore important to examine how the inference of other parameters is affected in both cases.

To obtain a more reasonable temperature structure incorporating the effect of clouds, we have to enforce a cloudy atmosphere with a free parameter  $\tau_{\text{cloud}}$ , which artificially sets the optical depth of the cloud at the photosphere of the clear component of the atmosphere (where the major emission contribution lies assuming no clouds). In this case, we no longer fit for the cloud mass fraction  $X_0^c$ . Instead, the optical depth of clouds at all pressure levels is scaled to fulfill the prescribed  $\tau_{\text{cloud}}$ . A strict prior is set to enforce optically thick clouds

( $\tau_{\text{cloud}} > 1$ ). Moreover, we also ensure that the prescribed  $\tau_{\text{cloud}}$  is physically plausible by constraining the scaling factor of the cloud optical depth to be less than  $2(f_{\text{sed}} + 1)$ . This factor  $f_{\text{sed}} + 1$  results from the requirement that the cloud surface density (i.e. integrating the product of density with cloud mass fraction vertically) be constrained by the available mass above the cloud base before condensation takes place (i.e. with the equilibrium mass fraction  $X_{\text{eq}}^c$ ). With the cloud mass fraction depending on the altitude via  $X^c(P) \propto P^{f_{\text{sed}}}$ , this leads to the constraint for the mass fraction at the cloud base:  $X_0^c \leq X_{\text{eq}}^c (f_{\text{sed}} + 1)$ . We added a factor of two to offer some flexibility.

This alternative model results in more pronounced clouds and less isothermal T-P profiles, as is shown in Fig. 3.4. Comparing the retrieved values of other atmospheric properties (see Table 3.2), we note that the atmospheric gravity and radius are significantly modified as a result of the heavy cloud and the altered temperature structure. The alternative model no longer probes as deep as the cloudless model because the clouds hide the region below. In addition, the metallicity becomes smaller when clouds are enforced in the retrieval, because the steeper temperature gradient requires less absorbing gas to achieve a similar absorption in emergent flux, as also explained in Burningham et al. (2021). Retrievals over a larger wavelength coverage (in particular, probing silicate absorption features at  $10 \mu\text{m}$ ) will reveal the nature of clouds and help better constrain other properties of the atmospheres (Burningham et al., 2021). Nevertheless, it is reassuring that the retrieval of the C/O and  $^{12}\text{CO}/^{13}\text{CO}$  ratios does not strongly rely on the accurate inference of temperature structure and clouds, which was also found in Mollière et al. (2020) and Burningham et al. (2021).

### 3.4.2 $^{13}\text{CO}$ detection

To reveal the presence of  $^{13}\text{CO}$  signal, we compare the observed spectrum to the retrieved best-fit model ( $\log(g)=4.69$ ,  $[\text{Fe}/\text{H}]=0.2$ ,  $\text{C}/\text{O}=0.55$ , and  $^{12}\text{CO}/^{13}\text{CO}=97$ ) in Fig. 3.1, and calculate the cross-correlation function (CCF) between the residuals (the observed spectrum minus the best-fit model without  $^{13}\text{CO}$ ) and a  $^{13}\text{CO}$  model (Fig. 3.2). The  $^{13}\text{CO}$  model spectrum is constructed by taking the difference between the best-fit model and the same model with the  $^{13}\text{CO}$  abundance set to zero. As is shown in the right panel of Fig. 3.2, the CCF peaks at zero radial velocity, signifying the detection of  $^{13}\text{CO}$  at a S/N of 8.4. This value varies slightly depending on the choice of velocity ranges where the standard deviation of the noise is measured.

We also determined the significance of the  $^{13}\text{CO}$  detection using Bayesian model selection. We performed the retrieval again while excluding  $^{13}\text{CO}$  opacity and the parameter  $^{12}\text{CO}/^{13}\text{CO}$ . Comparing its Bayesian evidence ( $Z$ ) to that of the full model (as listed in Table 3.3) allows us to assess the extent to which the model including  $^{13}\text{CO}$  is favoured by the observations. In Bayesian model comparison, the Bayes factor  $B_m$  (calculated by the ratio of  $Z$ ) is used as a proxy for the posterior odds ratio between two models. We then translated  $B_m$  to the frequentist measures of significance following Benneke & Seager (2013). As a result, the difference of  $\ln(Z)$  between two models is  $\Delta \ln(Z) = \ln(B_m) = 44$ , meaning that the observation favours the full model (including  $^{13}\text{CO}$ ) at a significance level of  $9.5\sigma$ . The detection remains the same significance ( $9.5\sigma$ ) when we use the alternative model with enhanced clouds.

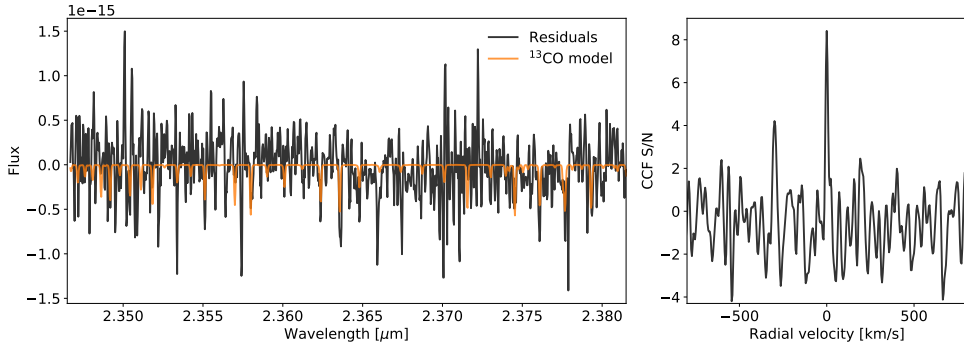


Figure 3.2: Left panel: observational residuals (observed spectrum minus best-fit model with the  $^{13}\text{CO}$  abundance set to zero) in black and  $^{13}\text{CO}$  model spectrum given the best-fit  $^{12}\text{CO}/^{13}\text{CO}$  ratio ( $\sim 97$ ) in orange. Right panel: cross-correlation function (CCF) between the  $^{13}\text{CO}$  model and residuals. The CCF is normalised by its standard deviation within the velocity ranges  $[-2200, -800]$  and  $[800, 2200]$   $\text{km s}^{-1}$ , so that the y-axis represents the signal-to-noise of the CCF peak.

Table 3.3: Results of Bayesian model comparison for the two retrieval models with and without  $^{13}\text{CO}$ .

Model	$\ln(Z)$	$\chi^2_{\text{best-fit}}$	$\ln(B_m)$
Full model	-1181	2372	44 ( $\sim 9.5\sigma$ )
$^{13}\text{CO}$ excluded	-1225	2470	-

$Z$  denotes the Bayesian evidence,  $\chi^2_{\text{best-fit}}$  the best-fit  $\chi^2$ , and  $B_m$  the Bayes factor.

### 3.4.3 Hint of $\text{C}^{18}\text{O}$

The observed spectra at 2.32-2.37  $\mu\text{m}$  and the best-fit model are shown in panel a in Fig. 3.5. The retrieved posterior distribution of the isotope ratios are shown in panel c and d. The cross-correlation functions (CCF) with the  $^{13}\text{CO}$  and  $\text{C}^{18}\text{O}$  templates are shown in panel b. We confirmed the previous detection of  $^{13}\text{CO}$  as suggested by the CCF peak at zero velocity, and obtained a consistent and tighter constraint on the carbon isotope ratio  $^{12}\text{CO}/^{13}\text{CO} = 108 \pm 10$ . As for the oxygen isotope ratio, the retrieval provided a tentative constraint of  $^{16}\text{O}/^{18}\text{O} = 1489^{+1027}_{-426}$ . The value is higher than the typical ratio ( $\sim 500$ ) found in the solar system or local interstellar medium (Wilson, 1999), while comparable to the measurements towards several young stellar objects (YSOs) (Smith et al., 2015) and an M dwarf binary (Crossfield et al., 2019b). We refrain from further interpretation of the provisional measurement of the oxygen isotope ratio, as we did not detect the  $\text{C}^{18}\text{O}$  in the cross-correlation analysis, indicating that  $\text{S/N} \lesssim 2$ . This is likely attributed to the lower than expected signal-to-noise ratio of the CRIFRES spectrum due to the far from optimal observing condition. Nevertheless, the tentative constraint of the oxygen isotope ratio in the brown dwarf suggests the prospect of exploiting the isotope inventory in sub-stellar objects with future data of higher quality.

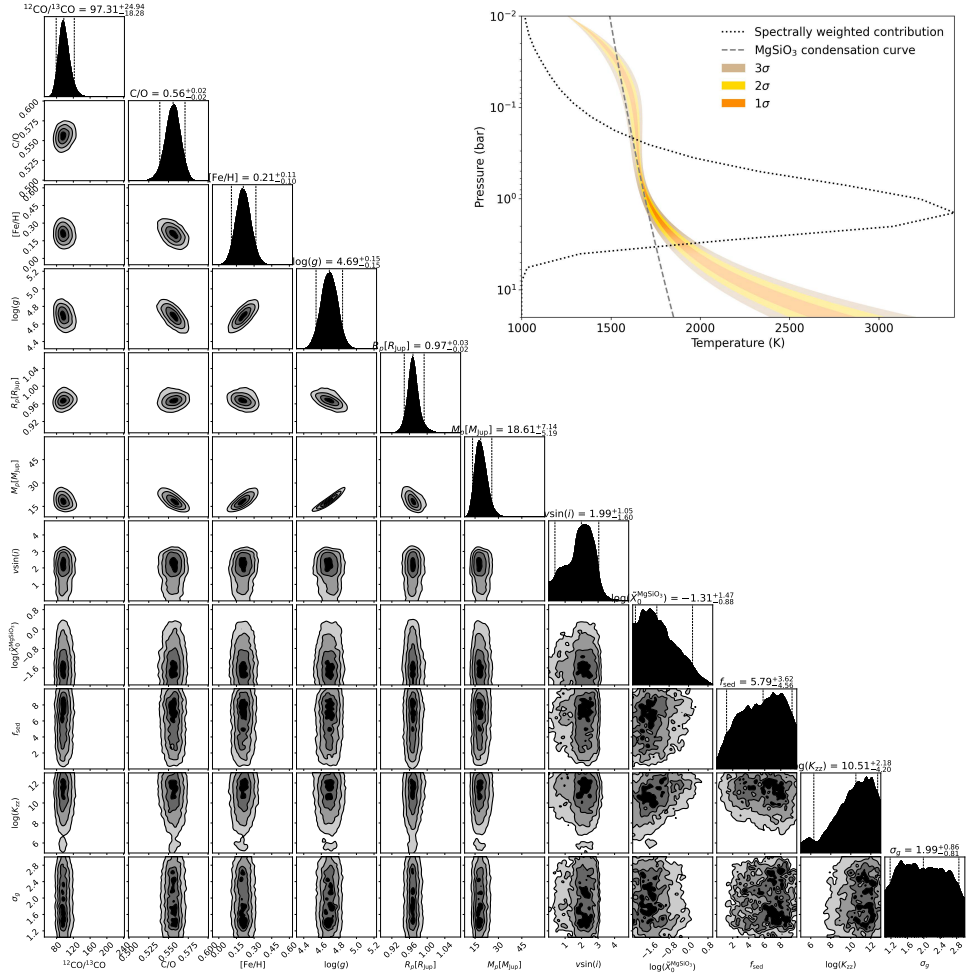


Figure 3.3: Retrieved parameters and temperature structure of 2M0355 using the nominal model. Upper right panel: retrieved temperature-pressure confidence envelopes. The coloured regions represent 1 $\sigma$ , 2 $\sigma$ , 3 $\sigma$  confidence envelopes. The black dotted line shows the flux average of the emission contribution function. The gray dashed line represents the condensation curve of MgSiO<sub>3</sub> clouds. Lower left panel: posterior distributions of parameters. The vertical dashed lines denote the 5%, 50%, 95% quantiles (90% uncertainties) of the distribution.

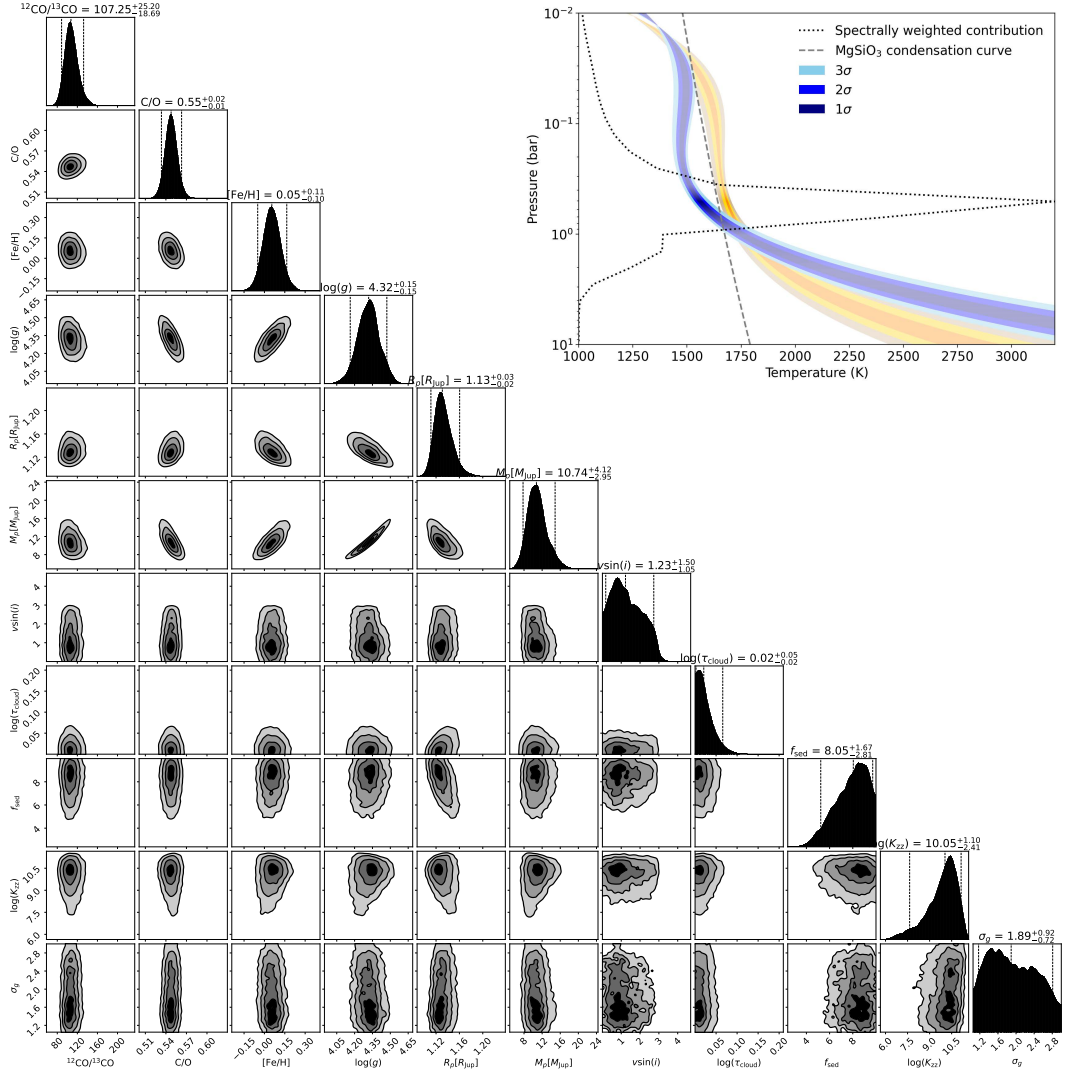


Figure 3.4: Similar to Fig. 3.3, but for the alternative model with enforced clouds. Upper right panel compares the temperature-pressure profiles of the nominal model in Fig. 3.3 (in orange) to this alternative model (in blue).

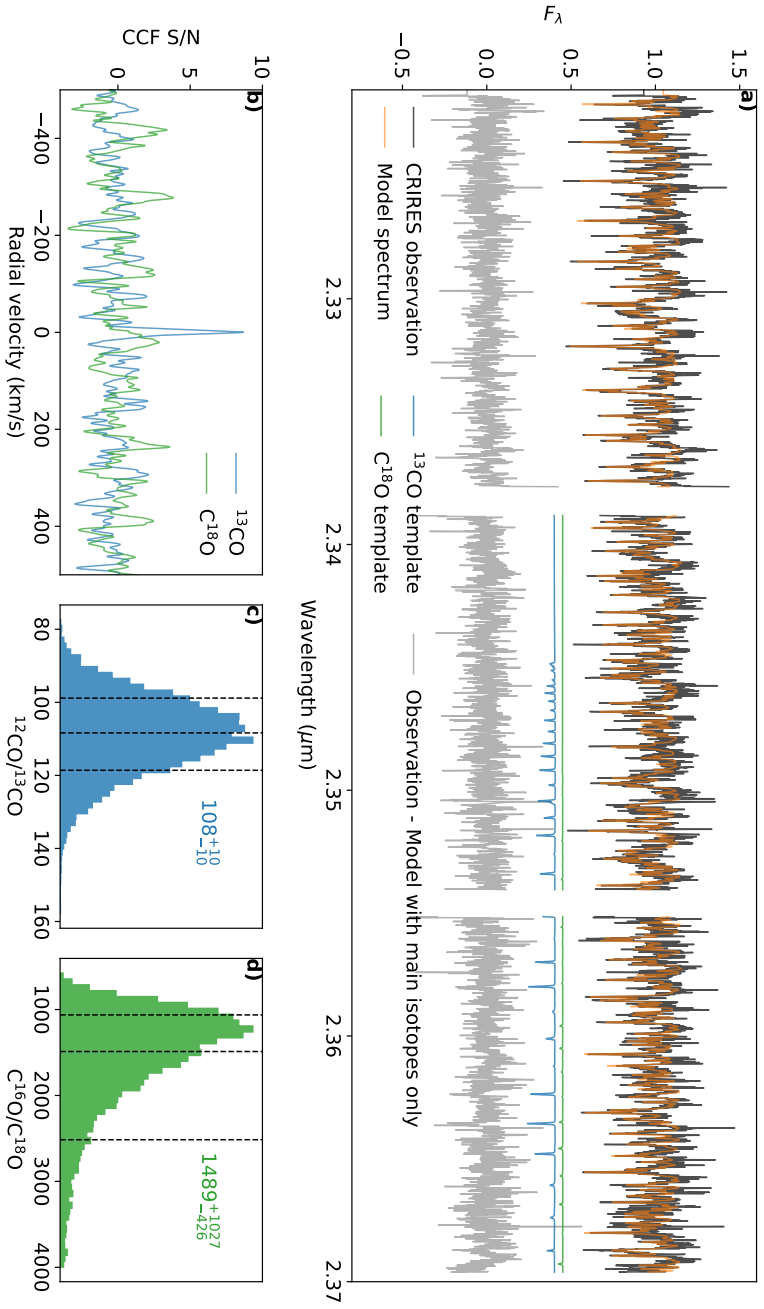


Figure 3.5: *Panel a)*: K-band (2.32-2.37  $\mu\text{m}$ ) spectrum of the brown dwarf 2M0355 taken with VLT/CRIFES. The orange line shows the best-fit model obtained through the retrieval analysis. The blue and green lines are the template spectra of  $^{13}\text{CO}$  and  $\text{C}^{18}\text{O}$ . The observational residuals (namely, observations minus the model with main isotopes only) are shown in gray. *Panel b)*: Cross-correlation functions of the observational residuals with the  $^{13}\text{CO}$  or  $\text{C}^{18}\text{O}$  template. *Panel c)*: Posterior distribution of the carbon isotope abundance ratio constrained by the retrieval. The vertical dashed lines denote the  $1\sigma$  interval. *Panel d)*: Same as *panel c)*, but for the oxygen isotope ratio.

## 3.5 Discussion

### 3.5.1 CO isotopologue ratio in 2M0355

We found the CO isotopologue ratio in 2M0355 ( $^{12}\text{CO}/^{13}\text{CO} = 97^{+25}_{-18}$ ) to be similar to the carbon isotope ratio measured in for the Sun ( $93.5 \pm 3$  by Lyons et al., 2018), while it is marginally higher than the ratio in today's local ISM ( $68 \pm 15$  by Milam et al., 2005), which is expected to be inherited by young objects. However, recent measurements of carbon isotope ratios towards a sample of solar twins suggest a current local value of  $\sim 81.3$  (Botelho et al., 2020), which is within the uncertainty of our measurement. Therefore, it remains unclear whether the CO isotopologue ratio in 2M0355 is indeed higher than its local environment.

We note that high  $^{12}\text{CO}/^{13}\text{CO}$  ratios were also observed towards some diffuse clouds, molecular clouds and YSOs in the solar neighbourhood (Federman et al., 2003, Goto et al., 2003, Lambert et al., 1994, Smith et al., 2015). If the high  $^{12}\text{CO}/^{13}\text{CO}$  ratios in molecular clouds and YSOs do not result from observational biases, it may not be surprising that the brown dwarf 2M0355 might inherit the high ratio from a  $^{13}\text{CO}$ -diminished parent cloud. One possible explanation for the high ratios towards diffuse clouds is the isotope-selective photodissociation (Bally & Langer, 1982, van Dishoeck & Black, 1988, Visser et al., 2009). Because of the lower column density of the rarer isotopologue, the self-shielding of  $^{13}\text{CO}$  takes effect at a deeper layer in the cloud. Consequently,  $^{13}\text{CO}$  is preferably destructed by far-ultraviolet (FUV) radiation, increasing the  $^{12}\text{CO}/^{13}\text{CO}$  ratios in the ISM. However, this explanation is not as plausible for molecular clouds and YSOs, because these objects with high extinction are supposed to be well shielded from FUV radiation. The isotope-selective photodissociation is unlikely to significantly alter the globally isotopologue ratios (van Dishoeck & Black, 1988). Other hypotheses were also suggested, such as higher excitation temperature in  $^{12}\text{CO}$  than in  $^{13}\text{CO}$  resulted from photon trapping in  $^{12}\text{CO}$  rotational transitions (Goto et al., 2003), CO gas-to-ice reservoir partitioning (Smith et al., 2015), and ISM enrichment caused by ejecta from carbon-rich giant stars or supernovae (Crossfield et al., 2019b), but no general and conclusive interpretation.

### 3.5.2 Implications for planet formation

It is intriguing to compare the  $^{12}\text{CO}/^{13}\text{CO}$  measurements between the L dwarf 2M0355 ( $\sim 97$ ) and the wide-orbit exoplanet TYC 8998 b ( $\sim 31$  by Zhang et al., 2021a). Despite similarities in several aspects, the young super-Jupiter has possibly undergone a different formation pathway to the isolated brown dwarf, leading to the difference in isotopologue ratio in their atmospheres. While isolated brown dwarfs may experience a top-down formation via gravitational collapse (which resembles star formation) or disk instability (Boss, 1997, Kratter & Lodato, 2016), super-Jupiters possibly form through the bottom-up core-accretion (of planetesimals and pebbles) (Lambrechts & Johansen, 2012, Pollack et al., 1996). Previous demographics on giant planets and brown dwarfs (Bowler et al., 2020, Nielsen et al., 2019) also support the two distinct formation pathways. As argued in Zhang et al. (2021a), the core-accretion scenario could possibly lead to  $^{13}\text{CO}$  enrichment through ice accretion, lowering the  $^{12}\text{CO}/^{13}\text{CO}$  ratio in observed super-Jupiter atmospheres.

Admittedly, it is preliminary to draw any conclusive interpretation based on a sample of two objects. Another caveat is that the two measurements towards the super-Jupiter



and the L dwarf are carried out under different spectral resolutions. It is so far unclear whether a smaller spectral resolving power can lead to any observational biases because it probes unresolved molecular lines. This calls for more future observations that enable homogeneous comparisons between different objects, in order to better understand the potential and limitations of carbon isotopologue ratio as a tracer for planet formation. It is also essential to interpret the isotopologue measurements in light of carbon fractionation in protoplanetary disks (Miotello et al., 2014), disk evolution (Trapman et al., 2021), CO ice chemistry (Krijt et al., 2020), and planet formation (Cridland et al., 2020), in order to provide constraints on the birth location, the relative importance of ice accretion, and possible vertical gas accretion processes during formation.

### 3.6 Conclusion

We analysed archival high-resolution spectra (from 2.275 to 2.385  $\mu\text{m}$ ) from Keck/NIR-SPEC of the isolated brown dwarf 2M0335 and carried out a free retrieval analysis. After removing the retrieved best-fit model that includes only the main isotopologues, we detected a  $^{13}\text{CO}$  signal using the cross-correlation method with a S/N of  $\sim 8.4$ . The detection significance was determined to be  $\sim 9.5\sigma$  with a Bayesian model comparison between the two retrieval models including or excluding  $^{13}\text{CO}$ . The isotopologue ratio  $^{12}\text{CO}/^{13}\text{CO}$  is inferred to be  $97^{+25}_{-18}$ , similar to the value found in the Sun, while marginally higher than the local ISM standard. If this deviation is real, it is possibly inherited from its parent cloud that has a high  $^{12}\text{CO}/^{13}\text{CO}$  ratio.

Although based on only two objects, it is also intriguing to note the difference between carbon isotopologue ratios in giant exoplanets and brown dwarfs, potentially implying distinct formation pathways. Despite spectroscopic similarities, brown dwarfs may experience a top-down formation via gravitational collapse, which resembles star formation, while giant exoplanets likely form through a bottom-up accretion process, which may alter isotopologue ratios in their atmospheres with dependencies on the accretion location and pathway in protoplanetary disks. This further emphasises the atmospheric carbon isotopologue ratio as a tracer for planet formation history. In the future, such an analysis can be implemented on spectra of more exoplanets to measure the carbon isotopologue ratios in their atmospheres and shed light on the location and mechanisms of planet formation.